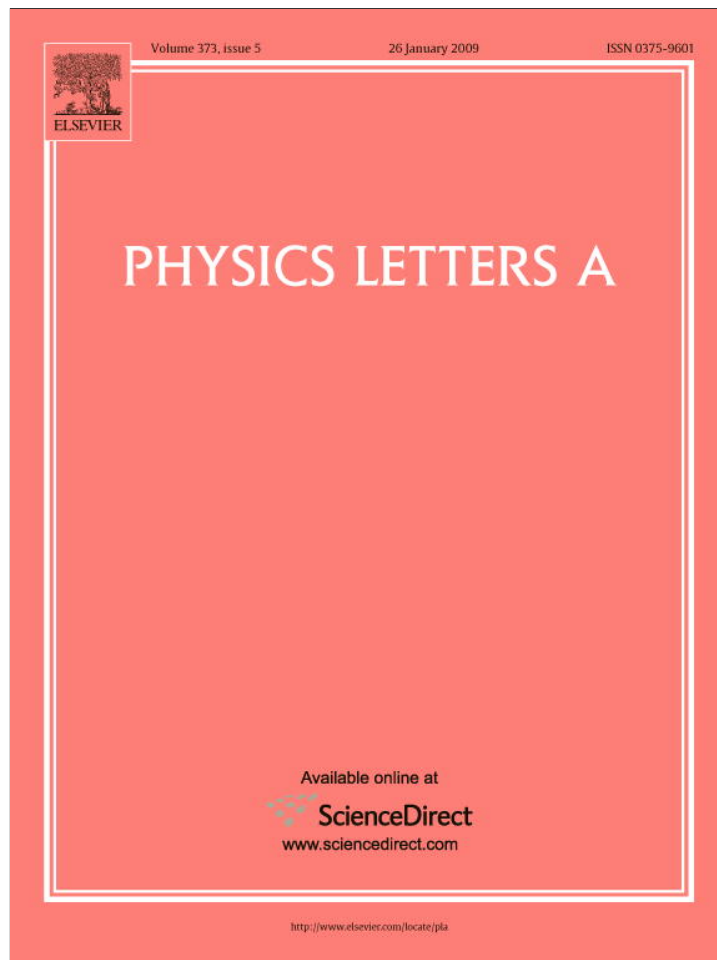


Provided for non-commercial research and education use.
Not for reproduction, distribution or commercial use.



This article appeared in a journal published by Elsevier. The attached copy is furnished to the author for internal non-commercial research and education use, including for instruction at the authors institution and sharing with colleagues.

Other uses, including reproduction and distribution, or selling or licensing copies, or posting to personal, institutional or third party websites are prohibited.

In most cases authors are permitted to post their version of the article (e.g. in Word or Tex form) to their personal website or institutional repository. Authors requiring further information regarding Elsevier's archiving and manuscript policies are encouraged to visit:

<http://www.elsevier.com/copyright>



Contents lists available at ScienceDirect

Physics Letters A

www.elsevier.com/locate/pla



Femtosecond index change mechanisms and morphology of SiC crystalline materials

Logan DesAutels^{a,*}, Christopher Brewer^b, Peter Powers^c, Mark Walker^g, David Tomlin^d, Albert Fratini^f, Shane Juhl^b, Weibin Chen^e

^a Wright–Patterson AFB, Air Force Research Laboratory, Materials and Manufacturing Directorate, AT&T Government Solutions Inc., Dayton, OH 45433, USA

^b Wright–Patterson AFB, Air Force Research Laboratory, Materials and Manufacturing Directorate, Dayton, OH 45424, USA

^c Electro-Optics and Physics Departments, University of Dayton, Dayton, OH 45469, USA

^d Wright–Patterson AFB, Air Force Research Laboratory, Materials and Manufacturing Directorate, UES Inc., Dayton, OH 45433, USA

^e Electro-Optics Graduate Program, University of Dayton, Dayton, OH 45469, USA

^f Chemistry Department, University of Dayton, Dayton, OH 45469, USA

^g Wright–Patterson AFB, Air Force Research Laboratory, Materials and Manufacturing Directorate, General Dynamics Information Tech., Dayton, OH 45431, USA

ARTICLE INFO

Article history:

Received 21 November 2008

Accepted 29 November 2008

Available online 6 December 2008

Communicated by V.M. Agranovich

ABSTRACT

Femtosecond lasers have a unique ability of processing bulk transparent materials for various applications such as micromachining, waveguide manufacturing, and photonic bandgap structures just to name a few. These applications depend on the formation of micron or submicron size features that are known to be index modifications to the bulk substrate [H. Guo, H. Jiang, Y. Fang, C. Peng, H. Yang, Y. Li, Q. Gong, J. Opt. A: Pure Appl. Opt. 6 (2004) 787]. To the best of our knowledge the physical understanding of how these index-modified features are formed is still unknown, but many good theories exist such as Petite et al. [G. Petite, P. Daguzan, S. Guizard, P. Martin, in: IEEE Annual Report Conference on Electrical Insulation and Dielectric Phenomena, vol. 15, IEEE, 1995, pp. 40–44] or Tien et al. [A. Tien, S. Backus, H. Kapteyn, M. Murnane, G. Mourou, Phys. Rev. Lett. 82 (1999) 3883]. In this Letter the question on the physical cause for index changes is investigated by the combined efforts between Wright–Patterson AFB (WPAFB) and the University of Dayton (UD) using numerous imaging equipment such as TEM, AFM, NSOM, Nomarski microscopy, X-ray crystallography, Raman spectroscopy, and even diffraction efficiency experiments. With all the combined imaging equipment this research is able to present valuable data and deduce plausible theories of the physics of the index modification mechanism.

© 2008 Elsevier B.V. All rights reserved.

1. Introduction

The morphology and the physical mechanisms for index changes of micromachined grating lines processed in crystalline transparent bulk materials; 6H-SiC semi-insulating and conducting samples were previously studied [1,2]. Following on the previous work, this Letter explores in greater depth in physical mechanisms for this transformation. Here, grating structures were micro-machined in 6H-SiC semi-insulating (SI) and 6H-SiC conducting then were analyzed with all of the following techniques: TEM, AFM, NSOM, Nomarski microscopy, X-ray Crystallography, Raman spectroscopy, and diffraction efficiency measurements. Each section then discusses the techniques used to image and analyze the processed areas. The conclusion gives a collective view of what the best hypothesis is for the mechanism responsible for creating an index

modification in bulk transparent crystalline materials using a single fs anamorphic laser pulse.

Our method of micromachining gratings uses an anamorphic lens designed to redistribute the ultrafast (UF) laser pulse from a 5.5 mm round Gaussian distribution to a 3 μm by 190 μm line shape [1]. Each individual grating line consists of three separate 190 μm lines exposed in sequence along the x -direction and 25 lines in the vertical, equating to $\sim 500 \mu\text{m} \times 500 \mu\text{m}$ grating. These gratings are typically about 1 μm to 10 μm deep below the surface depending on the focus alignment of the anamorphic lens. Fig. 1 shows a 500 $\mu\text{m} \times 500 \mu\text{m}$ grating in semi-insulating SiC with a spacing of 20 μm .

For these images, the optical microscope used is a NIST traceable Olympus upright digital BX51 microscope with Nomarski DIC (Differential Interference Contrast) capabilities that use high contrast prisms to produce increased contrast/resolution while the microscope is in reflection mode. The optical microscope reveals that the predicted line spread was found experimentally to be 5.5 μm wide \times 210 μm long for the semi-insulating SiC sample with a

* Corresponding author.

E-mail address: ld@loganopticaldesign.com (L. DesAutels).

~1–2 μm deep subsurface grating protruding above the surface, but a 3.5 μm wide \times 190 μm long grating for a ~5–10 μm subsurface grating. Thus, the optical microscopy gives two results on the morphology of these grating structures. One is that an index modification is revealed since the Nomarski DIC contrast difference is a result of or depicting any changes in the index of refraction. The second is the size of the structures and compared to the Zemax geometrical results. Due to the multi-photon process the intensity/fluence controlled mechanism is in close contrast to the geometrical results.

2. Atomic force microscopy

Atomic Force Microscopy, AFM was used to show the morphology of the surface (or 1–4 μm subsurface protruding structures) gratings micro-machined in semi-insulating (SI) and conducting 6H-SiC. The AFM used is a Veeco Dimension 3100 with a Nanoscope 3a controller in tapping mode to evaluate the topography of line distributions fabricated just above the threshold. Fig. 2 gives the results of the AFM for both SI and conducting SiC samples. The grating structures shown were not continuous (gaps between the grating lines) in order to show the morphology better.

The conducting SiC morphology is quite different than the semi-insulating (SI) SiC in that the material is obliterated causing pitting. While there is a discrete threshold for this obliteration in the conducting SiC, however, the widths of the obliterated lines were as predicted to the geometrical anamorphic lens morphology of 3 μm wide. In this case, the conducting SiC sample forms trenches that may be due to surface structural damage caused by thermal breakdown of the molecular lattice to the inability for the crystal to dissipate heat, and/or oxidation and chemical reactions

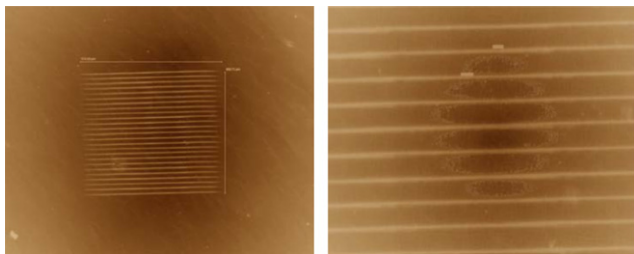


Fig. 1. (Left) SiC grating view with an optical microscope using Nomarski DIC for semi-insulating SiC on a 10 \times magnification; (right) 50 \times magnification. Image processing was performed in order to better resolve the modified surface lines.

on the surface that give a different compound. For, the SI SiC gratings, any surface modifications formed protruding “hills” which have a thicker width of 5.5 μm . This is most probably indicates a local subsurface restructuring has occurred or some other electronic trapping process [3] has forced the material to rise in the processed areas.

3. Transmission electron microscopy

TEM was performed on two types of grating structures made in semi-insulating SiC; one was subsurface and the second grating is just below the surface with a protruding “hill” as shown in the AFM section. These two gratings have fairly different TEM profiles, which is attributed to where they reside in relationship to the surface.

Fig. 3 shows a “dome” of lighter material which appears to be polycrystalline in the processed areas. The polycrystalline region is likely due to super cooling of the crystal lattice causing micro-

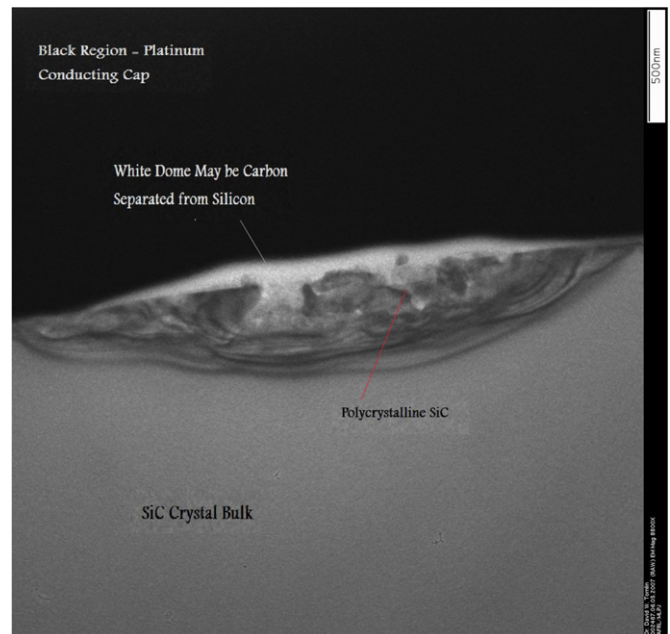


Fig. 3. Image of the surface grating TEM that is labeled to identify the key features of the TEM specimen.

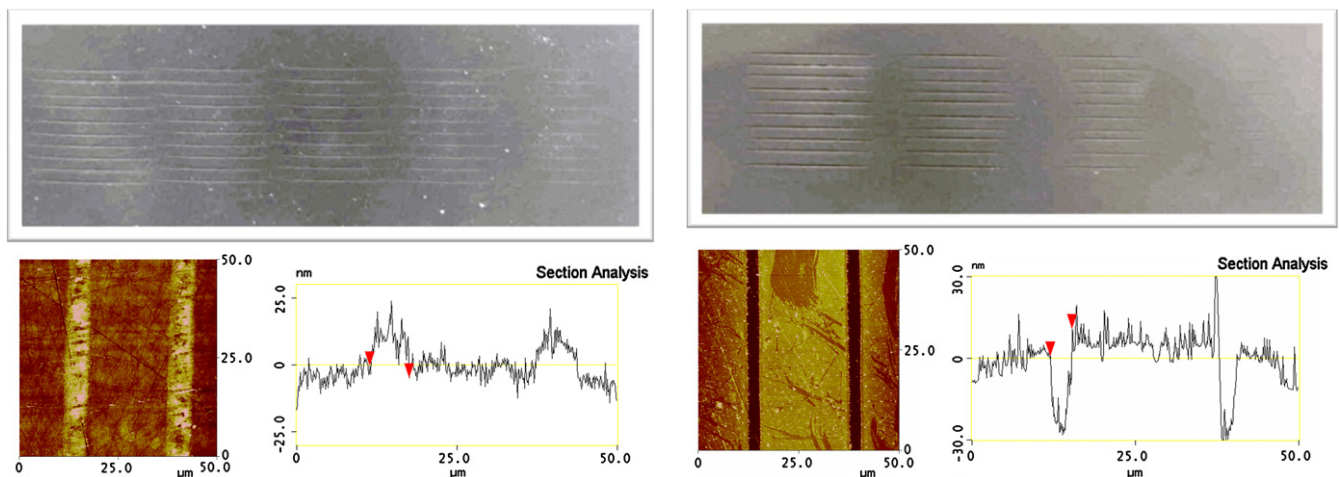


Fig. 2. (Left) shows the microscope DIC image of the semi-insulating SiC processed lines and AFM results of a 5.5 μm wide and a 10 nm raise surface modification on SI SiC material. (Right) shows the DIC microscope image of the conducting SiC sample and AFM results of a 3.0 μm wide and a 30 nm trench surface modification.

scopic crystalline regions that have random polarizations of the birefringent substrate. This is most likely a separation of carbon from silicon, causing the carbon to create a protrusion as shown in the AFM results. The “dome” is perceived to be carbon since Si has a larger atomic number typically appear darker in the resulting TEM imagery. The curved lines below the polycrystalline and above the SiC bulk is known to be caused by the electron beam diffraction affects from the TEM, which are of no consequence.

Next, TEM was performed on a subsurface grating micro-machined within the same semi-insulating SiC specimen. Fig. 4

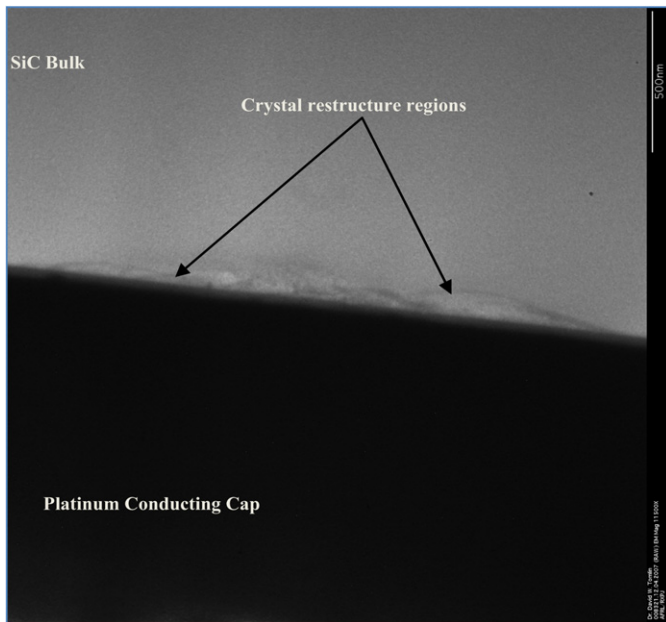


Fig. 4. TEM of subsurface SiC grating line.

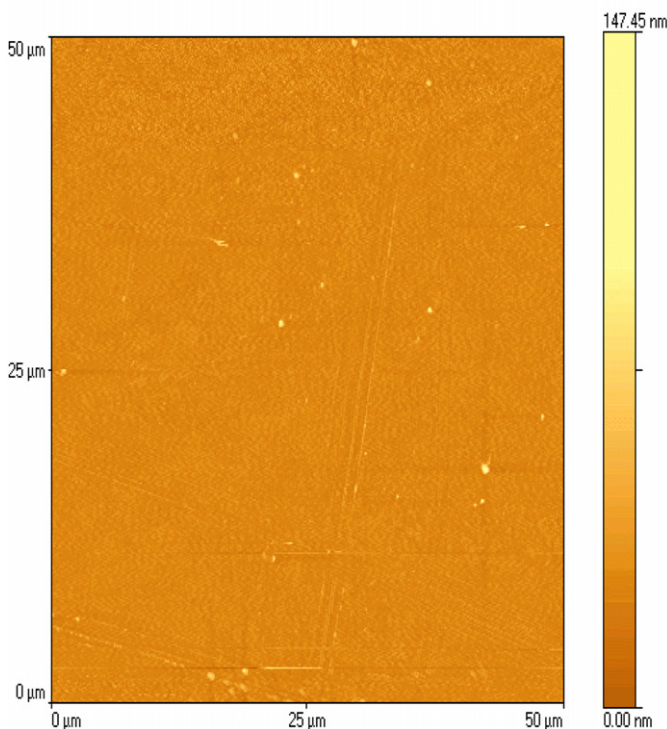
shows the TEM results for a subsurface semi-insulating 6H-SiC grating. As observed in this TEM the SiC bulk area is nearly the same color/density as the processed area, which suggests that the Si did not separate from the C and form polycrystalline. These results differ from that of the surface grating in that they do not have a separation of Si and C, or at least very little as is shown. Rather, it will be shown that the TEM results support a lattice deformation theory as will be described momentarily.

4. Near field scanning optical microscopy

NSOM is a technique used to assist in identifying whether the alterations are truly index changes. NSOM uses near-field diffraction where light is collected through the tiny tip of a fiber optic. The tip's entrance aperture can be on the order of tens of nanometers, and when the tip is brought to nanometers away from a sample under test, the resolution is not limited by far-field diffraction. The NSOM test was done on a semi-insulating subsurface SiC grating to ensure that the index change is due to phase modulations and not surface structures.

Fig. 5 gives the results of the NSOM optical image that is generated from a collimated light source illuminating the SiC sample (~250 μm thick) from the bottom while a fiber receiver collects the output from the top surface only, which is only ~100 nm from the surface. The topography image in Fig. 5 (Left) shows an absence of any surface alterations due to processing, but the modifications do exist below the surface. Fig. 5 (Right) demonstrates that the collimated input beam (from the bottom of the sample) is coming to a focus at the fiber receiver after propagating through the subsurface SiC grating line modifications. The grating lines act as micro-lenses consisting of convex radii and an index change in order to cause the collimated light to focus. The lighter areas in the optical image show where the light is coming to a focus at the fiber receiver, thus confirming the semi-insulating SiC sample con-

Grating 5: Topography



Grating 5: Optical

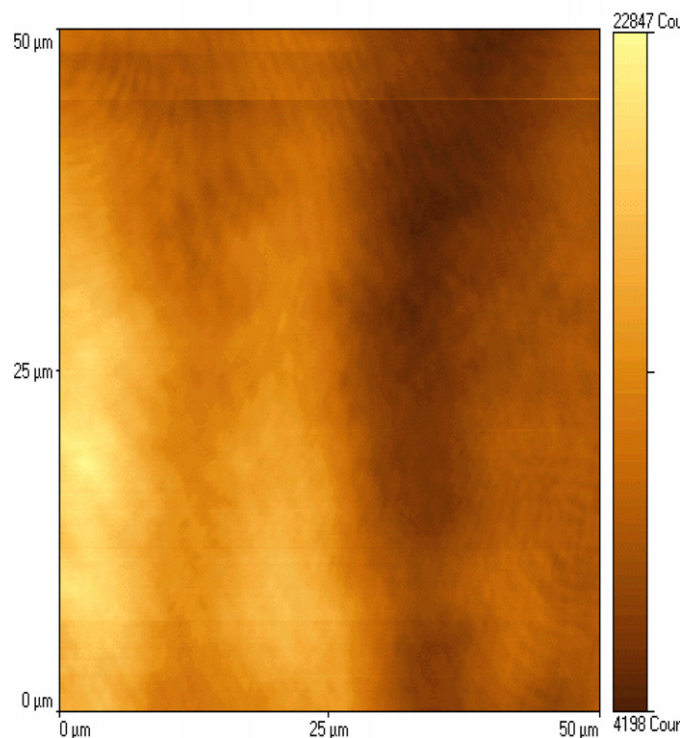


Fig. 5. (Left) is topography of the semi-insulating SiC sample; (Right) is the optical output revealing an index change.

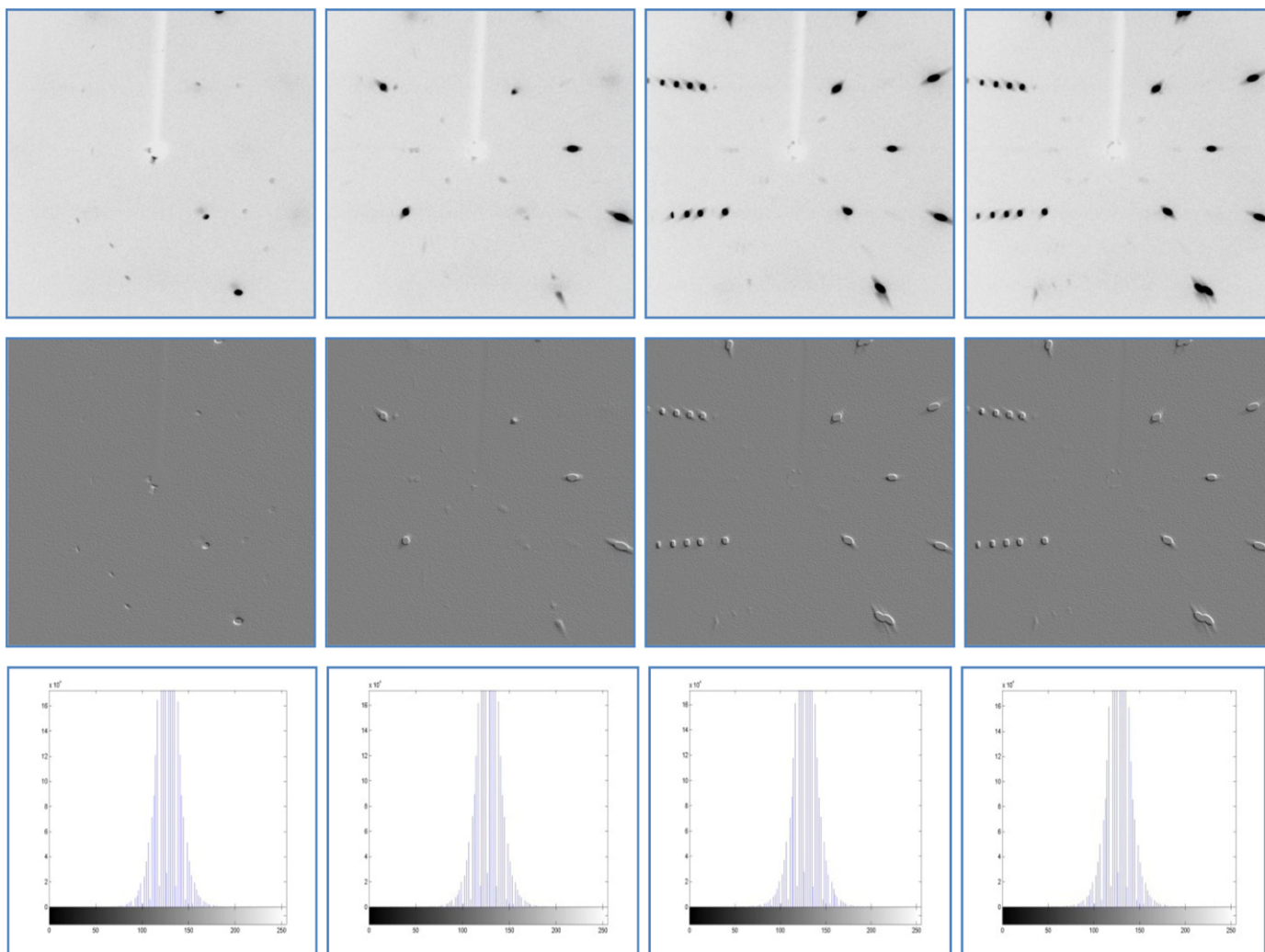


Fig. 6. Unprocessed SiC: in order from left to right—0°, 5°, 10°, and 15° scans. Top is the raw images, middle is emboss-processed raw images, and bottom are histograms of the emboss images.

tain a Δn only in the processed areas. The fact that this particular grating is subsurface also suggests that the modulation is phase and not amplitude.

5. X-ray crystallography

X-ray crystallography was performed on semi-insulating 6H-SiC to investigate any changes within the SiC crystal structure that might suggest the index of refraction modifications in this substrate are due to a change in the chemical structure of SiC either by broken bonds, new elements or impurities. A large area of the sample (about a 4 mm \times 4 mm area) needed to be processed for this technique due to the size of the X-ray analysis beam. Therefore, in order to process a large area, a long focal length spherical lens was used (250 mm focal length), which provided a 70 μ m focused spot diameter. To cover a large 4 mm \times 4 mm area a matrix of 70 μ m damage spots were produced with slight overlap of the spots to fully fill the area. Three different energy levels (40 μ J, 20 μ J, and 10 μ J) were used to create 3 different 4 mm \times 4 mm processed areas. The different energy levels provided various morphology on the SiC sample—from surface damage to subsurface damage were thus examined by this X-ray technique. In addition, an unprocessed area of the SiC was also tested to provide a reference or comparison for the processed areas.

The X-ray device used was the Oxford Diffraction Xcalibur 3 X-ray diffractometer (XRD). This is a fully-enclosed single crystal XRD system and has a Mo/Cu X-ray source with a Sapphire3 CCD detector. The instrument is computer-controlled with CrysAlisTM software for data analysis. Samples can be cooled to temperatures between 90 and 300 K with the Cryojet nitrogen jet cold unit. Each area on the 6H-SiC SI sample and tested was carefully aligned to the X-ray gun using the system CCD imager. The X-ray tests were setup for varying X-ray beam scanning at angles of 0° to 15°, with the sample initially set at \sim 45° to measure the X-ray diffraction off of the surface, and with a 10 second exposure time.

Figs. 6 and 7 show identical results for the processed and unprocessed areas. Similar results were also observed at the other energies. These findings suggest one of the following:

1. The SiC processed region has not been altered by the femtosecond radiation in a way of new bond structures or with any impurities introduced. The processed regions remain SiC crystalline.
2. The X-ray beam was “seeing” the bulk SiC and the processed areas’ modulation depths are not large enough volume to be resolved, but since the X-ray beam was incident onto the processed areas at a 45° angle it is unlikely that the beam is only interacting with the bulk SiC substrate.

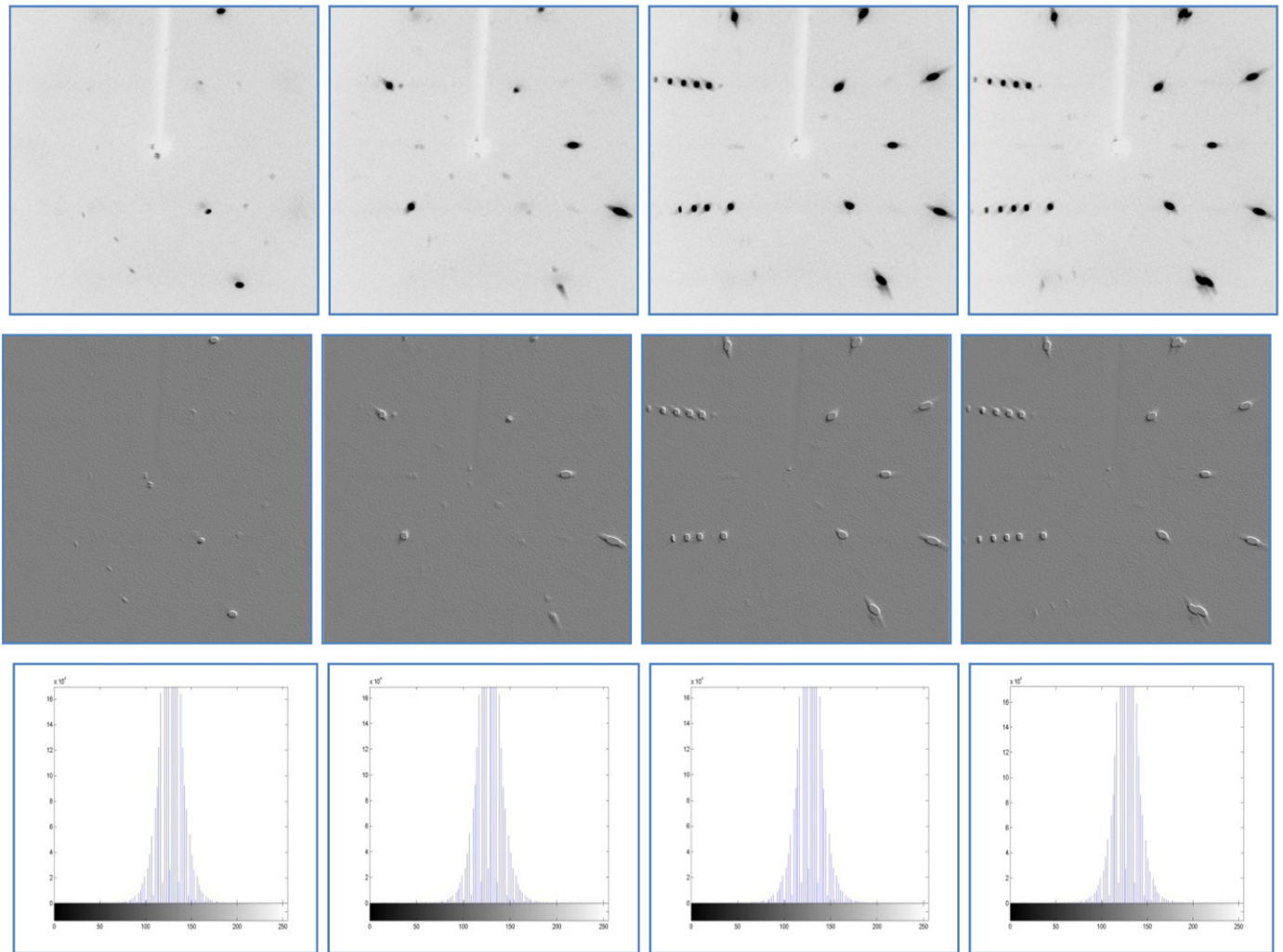


Fig. 7. Processed SiC for $E_1 = 40 \mu\text{J}$ area: in order from left to right -0° , 5° , 10° , and 15° scans. Top is the raw images, middle is emboss-processed raw images, and bottom are histograms of the emboss images.

6. Raman spectroscopy

Raman spectra were taken from both unprocessed and processed areas of semi-insulating 6H-SiC. As a baseline, the Raman data was also measured with fused silica and compared to referenced fused silica Raman results [4].

Fig. 8 illustrates the Raman spectra from SiC with the absence of fluorescence background contamination by using photo-bleaching and auto-baseline correction performed by the Raman instrument. The unprocessed semi-insulating (SI) 6H-SiC UD Raman was compared to a reference 6H-SiC Raman [5]. The Raman peaks are described by Burton et al. as an E_2 planar acoustic mode at 150.5 cm^{-1} , two planar optic or TO modes of E_2 symmetry at 767.5 cm^{-1} and 788.0 cm^{-1} , and an $A_1(\text{LO})$ phonon at 966.5 cm^{-1} . Burton et al. also mention that the mode at 796.0 cm^{-1} is a planar optical mode of E_1 symmetry, and there are two peaks around 500 cm^{-1} (505 and 513), which are A_1 axial acoustic LA modes [5].

Table 1 compares the Raman results for the unprocessed and processed 6H-SiC. This Raman spectrum suggests that a chemical change in the bond structure has not occurred since only the original 6H-SiC peaks exist. Instead broadened peaks more than likely represent a compression of the lattice atoms, which forces the dipoles to be in closer proximity with each other. Since the atoms are denser in the processed area, this causes a broadening of the Raman scattered peak.

The shift of the peaks may also represent a generation of phonons due to Brillouin scattering [7]. If the medium is compressed, from an external source such as a femtosecond laser pulse, its index of refraction changes and this is illustrated in Fig. 9 [6]. If the medium is compressed from an external source such as a femtosecond laser pulse, its index of refraction changes. Therefore, the shift in the 150 cm^{-1} E_2 planar acoustic, 766 cm^{-1} and 788 cm^{-1} E_2 planar optic, and the 966 cm^{-1} $A_1(\text{LO})$ SiC crystal lattice modes could suggest a deformation in the lattice [6]. The deformations change the dipole moments, where the photons now interact with these dipoles in their new locations which cause an effective index of refraction change.

7. Diffraction efficiency measurements

Grating structures were selected in order to measure the diffraction efficiency in semi-insulating 6H-SiC as a measure of performance over time and to approximate the change in index magnitude (Δn). The following measurement of the diffraction efficiency (η) was conducted to understand the quality of grating produced (how well the efficiency trends match theoretical grating trends) and to approximate the Δn knowing the measured η . The η was measured by varying the grating spacing, d , at constant energy/fluence. An example of a diffraction pattern is given

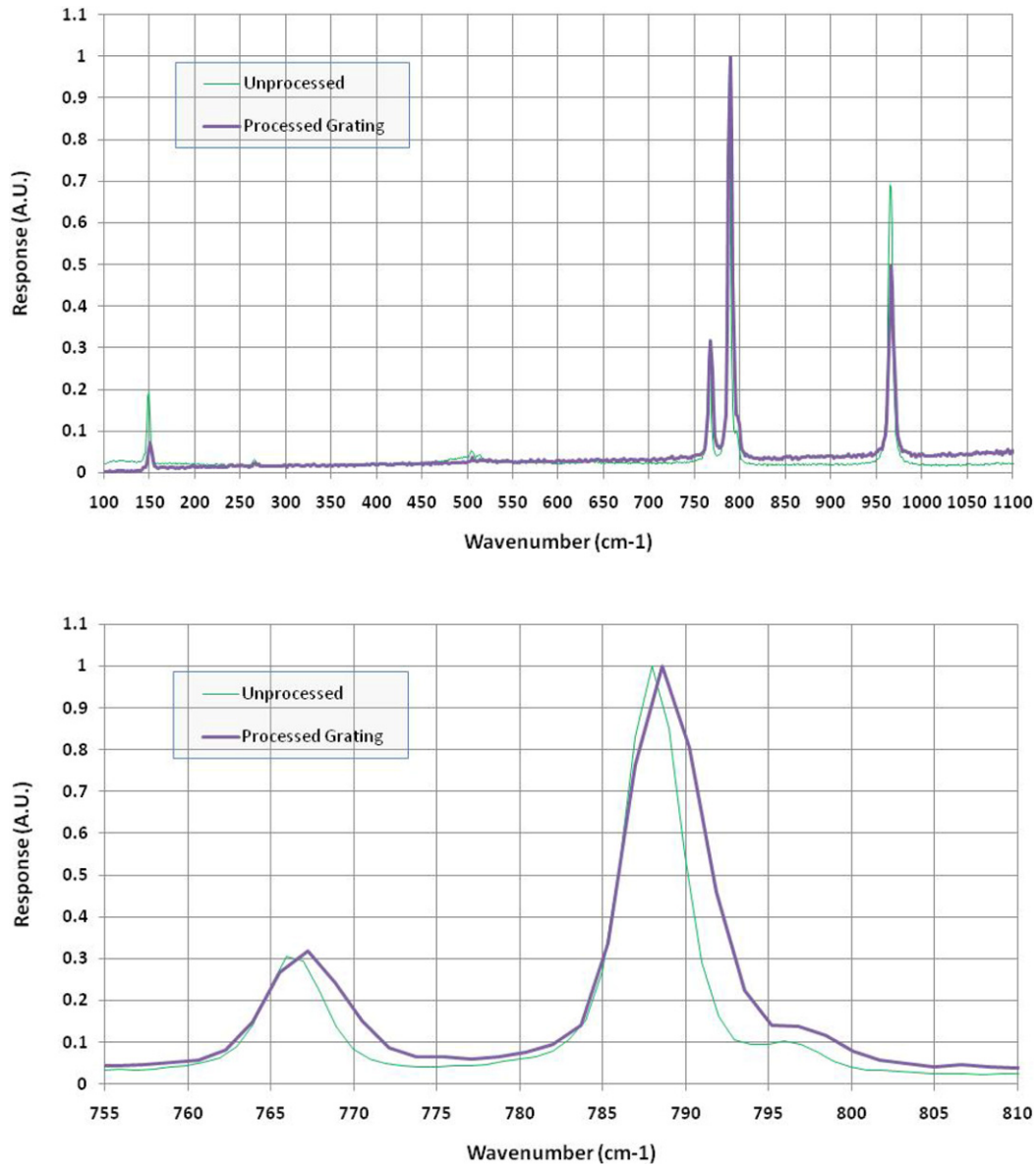


Fig. 8. (Top) University of Dayton Raman Spectra on semi-insulating processed and unprocessed SiC: Raman of processed and unprocessed 6H-SiC and is compared to a referenced 6H-SiC Raman from Burton et al. 6H-SiC Raman spectrum [5]. (Bottom) zoom of 766 cm⁻¹ and 788 cm⁻¹ peaks to illustrate the shift.

Table 1
Processed and unprocessed SiC peak analysis as shown in Fig. 8.

Unprocessed 6H-SiC peak Raman shift (cm ⁻¹)	Processed 6H-SiC peak Raman shift (cm ⁻¹)	Mode symmetry	FWHM broadening (cm ⁻¹)	Peak shift (cm ⁻¹)
148.5	149.34	E ₂ planar acoustic	1.0	0.84
505, 513	505, 513	A ₁ axial acoustic	0, 0	0, 0
765.9, 787.9	767.2, 767.2	E ₂ planar optic	2.6, 0.9	1.3, 0.7
965.5	966.25	A ₁ (LO)	1.5	0.75

in Fig. 10 to illustrate the complex pattern is formed from the micro-machined grating lines overlapping.

The top image in Fig. 10 shows the cross-section of a saturated profile of the diffraction pattern produced from a HeNe laser beam transmitting through a SiC grating. The image is saturated to allow a visualization of the structure between the peaks. This structure matches the theoretical profile as shown in the Bottom of Fig. 10. Here the theoretical diffraction pattern was calculated using a Fourier analysis of the grating structure as shown in Fig. 1. As mentioned, the grating structure consisted of three 3 μm × 190 μm lines in series that have a slight overlap of ~5–10 μm. This

overlap, the grating as a whole, and the square shape and size was considered in the Fourier analysis [8]. Eq. (1) gives the aperture transmittance function:

$$t_a(x, y) = \left[\left\{ e^{-\pi \left(\frac{x^2}{A^2} + \frac{y^2}{B^2} \right)} + e^{-\pi \left(\frac{(x \pm x_0)^2}{A^2} + \frac{y^2}{B^2} \right)} \right\} \otimes \left[\left\{ \left[\frac{1}{L} \text{comb} \left(\frac{y}{L} \right) \delta(x) \right] \text{rect} \left(\frac{y}{L} \right) \right\} \right] \right] e^{-\pi \frac{L^2}{\omega_0^2}} \quad (1)$$

The first two terms in this equation represent the femtosecond micro-machined processed anamorphic lines (3 lines) shifted from

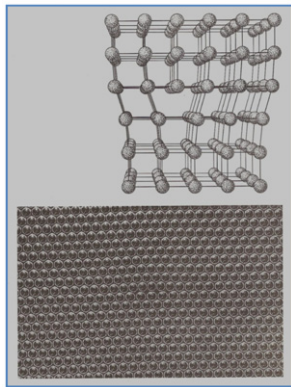


Fig. 9. Deformation of a crystal lattice that will cause a dislocation in the bulk medium, or an index of refraction change. This dislocation is seen in the center of the bottom image by tilting the page [6].

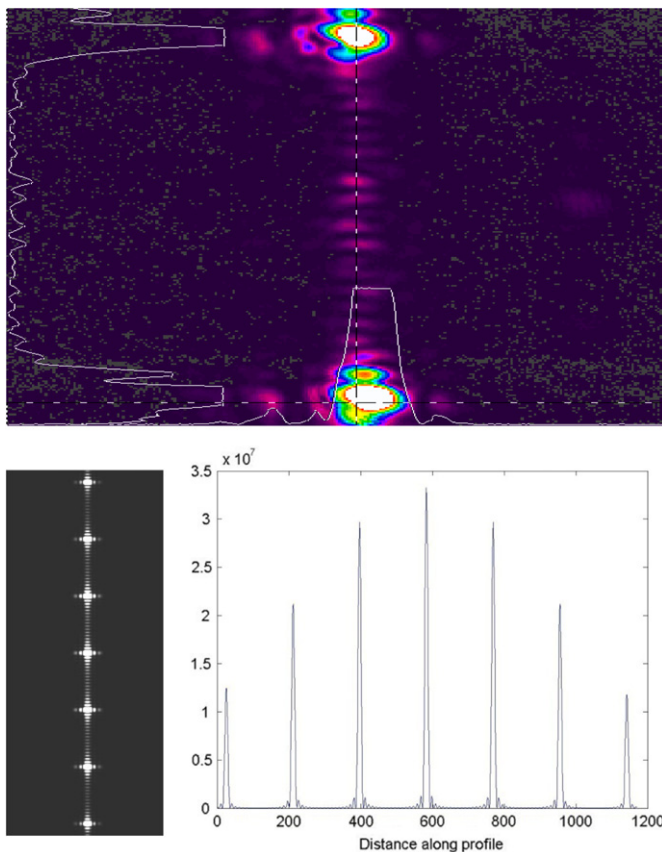


Fig. 10. Top shows SiC grating diffraction pattern using a Cohu 4812 CCD camera and Spiricon software, while bottom shows the same image only with using the Cohu 4812 CCD camera and Spiricon software.

x by $\pm x_0$, which is convoluted with the grating comb function and multiplied by the HeNe Gaussian function for spot size, ω_0 . The variables A and B represent the width and length of the processed grating lines, and L is the grating spacing. The rectangular (rect) function represents the grating width and length dimensions ($500 \mu\text{m} \times 500 \mu\text{m}$). Finally, the convoluted x and y terms are then multiplied by the HeNe Gaussian term.

The η output in Fig. 10 shows the 0-order and diffracted beams resulting from a HeNe laser at 632.8 nm, 1.5 mm $1/e^2$ beam diameter, and 1.5 mW output power. A long focal length lens was used to keep the HeNe beam diameter close to $500 \mu\text{m}$, which is roughly the size of the grating structures. The HeNe beam power and diameter were measured with Spiricon software and a Cohu

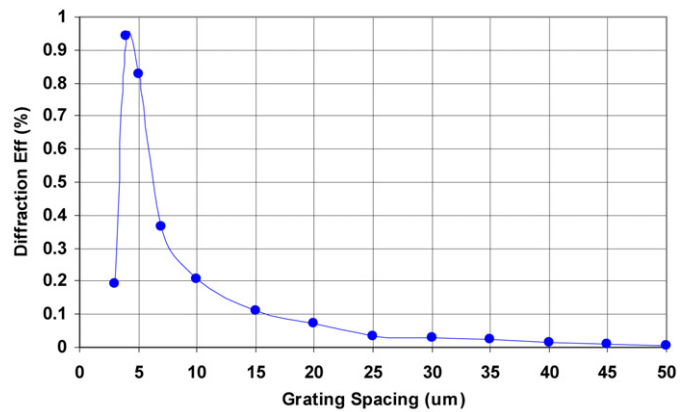


Fig. 11. η versus grating spacing.

4812 CCD camera in the absence of the gratings. The +1 and -1 orders were verified that they contained the same power within $\pm 5\%$. However, for the diffraction efficiency calculation only one of the orders were measured (the +1 order) and a factor of 2 inserted in the diffraction efficiency (η) calculation from Eq. (2).

$$\eta = \frac{2P_1 \cdot 10^{-(ND_0 - ND_1)}}{P_0} \cdot 100. \quad (2)$$

In Eq. (2), P_1 is the power of the 1st order measured beam, P_0 is the power of the zero-order beam, ND_0 is the neutral density filter OD placed in front of a Cohu 4812 camera when measuring the zero-order beam (no grating present only the unprocessed sample), and ND_1 is the neutral density filter OD placed in front of the Cohu camera while measuring the 1st order diffraction beam. Neutral density filters were needed to keep the CCD camera from saturating. P_1 and P_0 are measured using Spiricon laser beam analyzer (LBA) software with a Cohu 4812 CCD camera, which is calibrated using a Coherent FieldMax II TOP meter with an OP2-VIS detector (both traceable to NIST). The uncertainty in the diffraction efficiency measurement was determined using standard propagation of uncertainties and found to be $\pm 1\%$ for the meter accuracy and $\pm 4\%$ for the ND values, thus leading to an overall uncertainty in the diffraction efficiency of $\pm 5\%$.

Fig. 11 shows the diffraction efficiency of semi-insulating 6H-SiC is $\sim 0.08\%$ for grating spacing of $20 \mu\text{m}$, whereas for $d = 4 \mu\text{m}$ the maximum η is $\sim 0.95\%$ in the same semi-insulating SiC sample. For this study we specifically analyzed two efficiencies 0.08% and 0.46% for single and two pulses, respectively, using $20 \mu\text{m}$ spaced gratings.

In order to perform Δn magnitude calculations, the structure has to have only phase changes and not amplitude changes. As seen above, using NSOM, TEM, optical microscope (with Nomarski capabilities), and AFM it is possible to determine the type of grating that is written. A sample where only a sinusoidal phase change (subsurface machining) occurs is called volume phase holographic (VPH) gratings.

The diffraction efficiency, η , of a VPH grating for phase only modulation depends upon the thickness, L , the grating angle, β , with respect to the input beam, the wavelength, λ and Δn of the modulation; as defined by Barden et al. [9]. This approximation assumes a sinusoidal structure, which is an acceptable estimate for this analysis.

$$\eta = \sin^2 \left(\frac{\pi \Delta n \cdot L}{\lambda \cos(\beta)} \right). \quad (3)$$

Here β is defined as the Bragg angle and is given as [9]

$$\beta = \sin \left[\frac{n_{\text{air}}}{n_{\text{SiC}}} \sin(\alpha_i) \right], \quad (4)$$

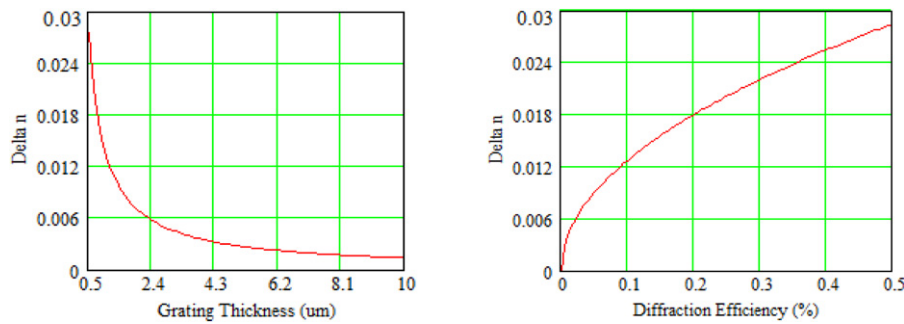


Fig. 12. (Left) Δn versus modulation depth; (Right) Δn versus diffraction efficiency.

where α_i is the incident angle of the input beam that is dependent on the HeNe laser alignment and how well the sample was aligned to the femtosecond laser during the micro-fabrication process. Also, n_{air} is the index of air which is 1.0, and n_{SiC} is the average index of ordinary and extraordinary indices of SiC. The extra-ordinary, n_e and ordinary, n_o indices are calculated using Shaffer et al. for 632.8 nm to be 2.677 and 2.639, respectively, which results in the average SiC index, n_{SiC} of 2.658 [10]. The incident angle is therefore estimated to be under 3° , which provides a Bragg angle of $\beta = 1^\circ$. The Bragg angle, β , and incident angle do not have a large affect on Δn ; approximately 0.8% difference in β from 0° to 20° .

Now, if Δn is solved from Eq. (3) above then we have

$$\Delta n = \sin^{-1}(\sqrt{\eta})\lambda \frac{\cos(\beta)}{\pi L}, \quad (5)$$

where Δn is found to be 0.011 to 0.027 for η of 0.08% to 0.46% (single and two pulses, respectively) and for $L = 0.5 \mu\text{m}$; L , as will be shown, is the modulation depth of the grating structures found using TEM. Next, using the above equations, the Δn was varied as a function of modulation depth. In addition, Δn was also plotted as a function of η ; both plots shown below.

As shown in Fig. 12 the trend of Δn increases as the modulation depth decreases, which means that the index change has to be greater in order to achieve the same diffraction efficiency for a smaller depth. Also Fig. 12 shows Δn increasing as efficiency increases, and shown is a Δn of 0.027 for $0.46 \pm 0.023\%$ efficiency.

8. Index modification degradation over time

Grating structures were micromachined in semi-insulating and conducting 6H-SiC as mentioned. These processed features were created in these samples over a 2–3 year span, and in that time most of the grating structures were re-investigated under the optical microscope numerous times for various reasons. It was during those periodic inspections that it was observed the SiC grating subsurface and surface structures were still present and had not degraded. These SiC crystalline materials were also processed and their features investigated over time and shown in Fig. 13.

As observed from Fig. 13, the SiC gratings have not degraded (or “healed”) to any significant amount. In fact, the SiC 2008 SiC grating image was also repeatedly annealed to 399°C . Thus, neither time nor heat will alter the SiC subsurface grating structures, which suggests their crystal structure was indeed altered and the lattice is different. This suggests (hypothesis) that the lattice dipoles are at different locations due to a deformed atomic lattice [6] and this would cause an index change given that when light interacts with those new dipole moments a new index of refraction is the result. However, surface modifications to the crystalline structure typically do not recover primarily because atomic

bonds have been broken and react with the atmosphere forming pits in the surface.

9. Summary of results

A summary of all of the above experiments is given to consolidate each conducted experiment to provide a better understanding of what the possible causes of femtosecond index modifications in crystalline and anamorphic materials. At the very least, the data provided will add to the science of index of refraction changes in bulk transparent materials. Below is a list of the key findings.

1. Optical microscopy:
 - a. Nomarski DIC images provide evidence that the subsurface features are resulting from phase changes within the bulk transparent substrate that are attributed to index of refraction changes.
2. Atomic force microscopy:
 - a. Surface SiC grating features resulted in protruding rises caused by the creation of a carbon-dome that should have a different index of refraction from that of the bulk due to possible broken Si–C bonds creating localized amorphous Si and/or C within the crystalline bulk.
 - b. Subsurface SiC grating features is the result of lattice deformation. Thus the primary cause for index change is likely crystal lattice dipole changes.
 - c. Surface SiC grating features likely are attributed to thermal breakdown of the molecular lattice.
3. X-ray crystallography:
 - a. No evidence of new elements or compounds was found in the processed SiC.
4. Raman spectroscopy:
 - a. No evidence of new elements or compounds was found in the processed SiC.
 - b. Some peaks have been broadened and shifted slightly, which is probably caused from crystal lattice deformation.
5. Transmission electron microscopy:
 - a. Support of the AFM results:
 - i. Surface SiC grating features resulted in protruding rises caused by the creation of a carbon-dome that should have a different index of refraction from that of the bulk.
 - ii. Subsurface SiC grating features resulted lattice deformation, thus the primary cause for index change is likely due to crystal lattice dipole changes.
 - b. The TEM results also provided the true grating modulation depth of $0.5 \mu\text{m}$.
6. Near scanning optical microscopy:
 - a. The subsurface SiC grating features have been proven to be below the surface and a phase-only index change.
7. Diffraction efficiency experiments:
 - a. For the subsurface gratings a phase only diffraction orders were created owing to $\eta \sim 0.5\%$.

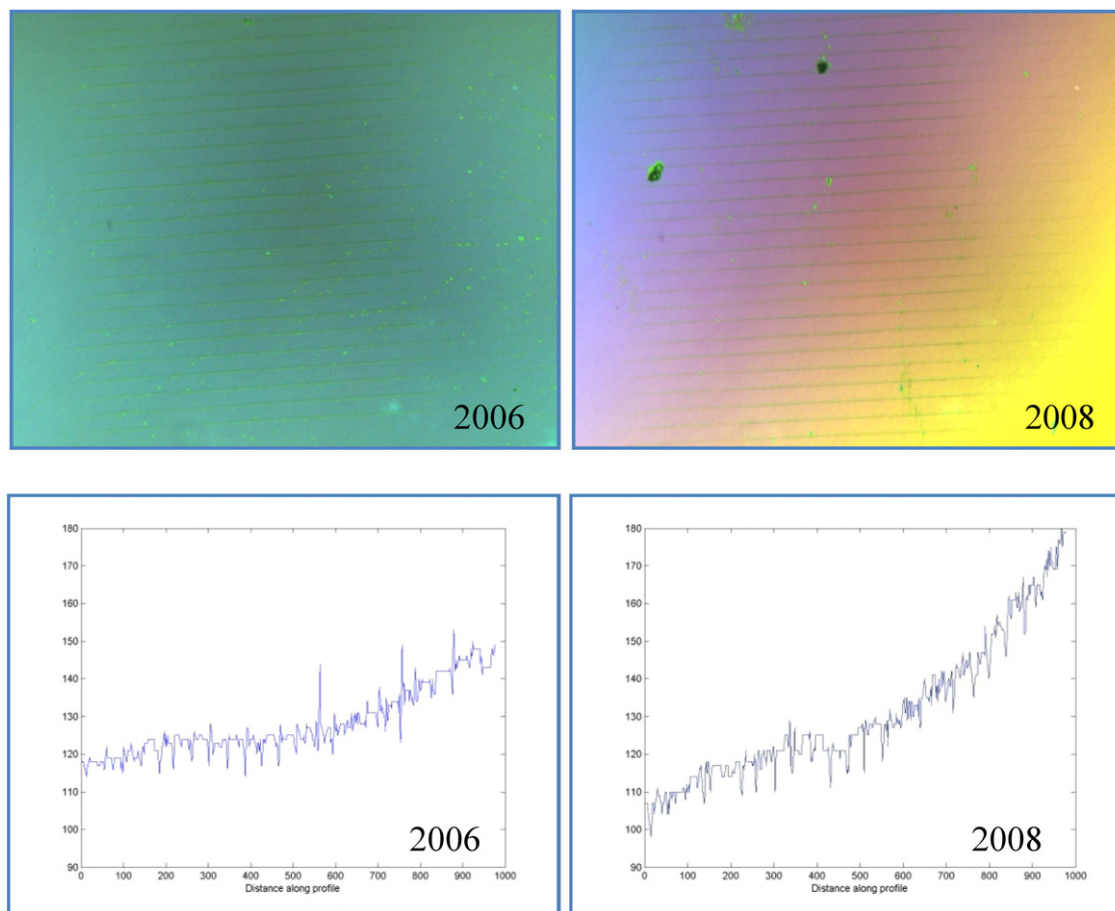


Fig. 13. Subsurface semi-insulating 6H-SiC gratings: (Top) are the optical microscope images, (Bottom) are the lineout images.

- b. The subsurface gratings also follow VPH theory as a function of diffraction angle and magnitude of $\Delta n = 0.011$ to 0.027 for single and two pulses, respectively.
 - c. For the surface gratings, phase and amplitude diffraction is the result.
8. Time study:
- a. These observations proved to be valuable in the fact that they provide support of the TEM, X-ray, and Raman measurements—no chemical alterations in the SiC, but rather a lattice deformation.

In conclusion, index changes that exist in SiC crystalline materials were studied. We suggest the crystalline subsurface index changes are likely due to the crystal lattice deformation. This is likely caused by the short-pulse multiphoton ionization process, which redistributes the electron dipoles to new locations from the deformed lattice and causes the incident photons to interact with these new dipoles resulting in a new index of refraction. There is no evidence of new elements, compounds, or impurities within the processed regions of the crystal. Surface crystalline index modifications are most probably due to localized broken bonds between Si and C causing a “carbon-dome” and/or randomly oriented polycrystalline resulting in average n_e and n_o indices. This work provides theories and scientific data from various imaging techniques consolidated in one article.

Acknowledgements

Special acknowledgements are given to the US Air Force Research Laboratory and the University of Dayton for making this research possible; also to Dr. Frank Baxley (WPAFB/AFRL/RV/General Dynamics) for his contribution to the lattice deformation theory.

References

- [1] L. DesAutels, C. Brewer, M. Walker, S. Juhl, M. Finet, P. Powers, *Opt. Express* 15 (20) (2007) 13139.
- [2] L. DesAutels, C. Brewer, M. Walker, S. Juhl, M. Finet, S. Ristich, M. Whitaker, P. Powers, *J. Opt. Soc. Am. B* 25 (2008) 60.
- [3] S. Mao, F. Quéré, S. Guizard, X. Mao, R. Russo, G. Petite, P. Martin, *Appl. Phys. A* (2004) 1695.
- [4] J.W. Chan, T. Huser, S. Risbud, D.M. Krol, *Opt. Lett.* 26 (21) (2001) 1726.
- [5] J. Burton, L. Sun, M. Pophristic, S. Lukacs, F. Long, Z. Feng, I. Ferguson, *J. Appl. Phys.* 84 (1998) 6268.
- [6] C. Kittel, *Introduction to Solid State Physics*, fourth ed., John Wiley and Sons, 1969, pp. 673–675.
- [7] R. Paschott, *Encyclopedia of Laser Physics and Technology*, http://www.rp-photonics.com/brillouin_scattering.html.
- [8] J.W. Goodman, *Introduction to Fourier Optics*, ISBN 0-9747077-2-4, Roberts and Company, 2005.
- [9] S. Barden, J. Arns, W. Colburn, J. Williams, *Publ. Astron. Soc. Pacific* 112 (2000) 809.
- [10] P. Shaffer, R. Naum, *J. Opt. Soc. Am.* 59 (1969) 1498.